Design and Instrumentation of a Novel Centrifuge Container for Fly Ash Run-out Experiments

Madabhushi, S.S.C, Martinez, A., Wilson, D.W. and Kutter, B.L.

Abstract

Debris flow, landslides and material run-outs have significant environmental and economic consequences for numerous industries. High quality experimental data with controlled boundary conditions can help validate and calibrate the predictive capabilities of mechanistic and semi-empirical numerical models. A novel centrifuge container to model dewatering and run-outs induced by a rapid loss of confinement is presented. The design features a pair of vertical doors opened in-flight to simulate failure of the containing structure. Illustrative centrifuge results investigating the run-out characteristics of a fully saturated, densely deposited class-F fly ash are presented. Modified soil moisture probes to monitor the distributions and time-varying fly ash water content throughout the testing are explored. Further, successful use of depth sensing cameras to reconstruct progressive deformations of the material front at various time scales is demonstrated. Combined water content, pore pressure and deformation measurements provides insight into the material behaviour during the run-out, revealing two-time scales at which the deformations occur. However, discrepancies between water contents inferred from the dielectric measurements and electrical conductivities highlights the need for independent verification of the bulk material water content when using the modified probes. Overall, the potential of these innovative instrumentation techniques to complement traditional geotechnical instrumentation is shown.

Keywords: Centrifuge modelling, Fly ash (PFA), Landslides, Slopes

1 Introduction

Large scale deformations or fluidized flow of saturated granular materials can have devastating economic and environmental impacts. A variety of different industries are concerned by such events, which can include landslides and debris flow such as in Sierra Leone, 2017 or in Hong Kong, 1990 (Bowman et al., 2010), the failures of tailings dams as with Mt Polley, 2014, Fundao, 2015 (Been, 2016) or Brumadinho, 2019 and the failure of fly ash impoundments such as Kingston, 2008 (Bachus et al., 2019).

In the case of saturated granular materials, the intrinsic coupling between the effective stresses, voids ratio and pore pressures can lead to dramatic changes of both the strength and stiffness as the material deforms and ultimately lead to larger total run-out distances. However, other phenomena or mechanisms have been theorized to impact the material run-out, including entrainment and mechanical or even acoustic fluidisation (Johnson et al., 2016), the generation of heat during large volumes of material shearing (Pinyol et al., 2018) or inter-granular lubrication (Delaney and Evans, 2014). McDougall (2017) presents a comprehensive review of different run-out analysis methodologies and the associated challenges, and distinguish between numerical models that are semi-empirical such as Rheological versus purely mechanistic models. It is noted that the former approach is more prevalent in practice though suffers from difficulty in determination of parameters that do not necessarily have an underlying physical basis, such as a visco-plastic parameters or constant residual shear strengths. For both approaches, there is a clear need for high quality physical data to help verify predicted material behaviours, mechanisms and the total run-out distances.

As part of a project investigating the impact of dewatering on the stability of fly ash ponds, a novel centrifuge container was developed at the 'Center for Geotechnical Modeling' (CGM) at the University of California Davis that can model the run-out behaviour of saturated granular materials (EPRI, 2021). In this paper, the design, instrumentation and example results from centrifuge tests on a fully saturated dense fly ash run-out are presented to showcase the insight into the mechanical behaviour that can be obtained.

Use of the large 9-m geotechnical centrifuge at the CGM to model the fly ash run-out is driven by recognition of the role of the effective stresses in the material constitutive behaviour. The centrifuge box is designed to model a rapid loss of confinement for the contained material by reducing the total horizontal stress on one face of the material. The design criteria, capabilities and practical considerations of the novel container are first discussed in this paper.

Appropriate instrumentation of the container and material is required to facilitate characterization of the material behaviour prior to and during the run-out test. The performance of low cost moisture content probes and depth sensing cameras is explored. For fine grained materials such as fly ash, the gravimetric water content of the material can influence the constitutive behaviour below and above the water table. For fully saturated materials, the water content can be treated as a proxy for the undrained shear strength and below the water table positive pore pressures will reduce the effective stresses. Further, the suctions that can develop above the water table can lead to non-linear effective stress increases following from the Soil Water Retention Curve (Bishop and Blight, 1963; Madabhushi et al., 2020). It is thus desirable to measure the soil water content in-flight, i.e. during the centrifuge test. Moisture content probes embedded in a material measure its electrical properties or characteristics that can be correlated to water content using a calibrated relationship (Kizito et al., 2008; Meter Group Inc., 2018). The consequences of the calibration results and

unique behaviour of the saturated class F fly ash tested will be discussed, and examples of the temporal variations and spatial distributions measured in conjunction with the pore pressures during centrifuge tests will be presented.

Obtaining the progressive run-out displacements of the material body in three dimensions provides direct insight into the material behaviour and associated bulk failure mechanisms, and further can be used to calculate net volume changes or movements. The total run-out distance is also often the critical design parameter of practical significance and a value that predictions from numerical studies are verified against. The performance of multiple inexpensive depth sensing cameras used to track the short and long term deformations of the fly ash, a relatively uniform and untextured material, will be presented in this paper.

2 Centrifuge Testing and Container Design

2.1 Introduction to reduced scale physical run-out modelling

Small scale modelling of run-out problems can provide an economic insight into the critical failure mechanisms. However, to enable more direct comparisons with full scale cases or for validation of numerical methodologies, the use of a geotechnical centrifuge facilitates testing of small scale models at comparable stress levels to the full scale case. The relationship between the small scale model behaviour on a centrifuge, i.e. subjected to a centrifugal acceleration increasing the stresses in the model, and the full scale behaviour, can be mapped using scaling laws (Schofield, 1980).

Scaling laws describe how a centrifugal acceleration of Ng on a small model will produce behaviour equivalent to a prototype case N $\times$ larger experiencing a vertical acceleration of 1 g, as the stresses and strains will be equivalent. Whilst linear dimensions and accelerations are straightforwardly scaled, the scaling of other parameters can require further consideration. For example, Bowman et al. (2010) discuss the scaling laws for debris flow in a geotechnical centrifuge. In that work, it was hypothesized that the time scaling for such processes can follow that employed for seismic loading, i.e. increased by a factor N, with the granular material in the model saturated with a pore fluid $N\times$ more viscous than the prototype case modelled. This ensures consistency between the inertial and diffusion scaling laws. In the present study, the fly ash tested was saturated with deionized water, i.e. pore fluid with the same viscosity to that in the full scale case. This was partly driven by the risk of viscous pore fluids with polymer chains such as methyl cellulose affecting the constitutive behaviour of fine grained materials such as fly ash. For simplicity, when time varying measurements are presented in this paper 'model time' will be used. The appropriate scaling of time for such tests will be discussed in future works.

Bryant et al. (2015) present a discussion on the influence of Coriolis accelerations on dry granular flows modelled using a centrifuge. When the lateral movement of the slope model is in the plane of rotation of the centrifuge, the Coriolis accelerations can affect the run-out distance. In the present studies modelling with the 9 m radius centrifuge at Davis, the primary lateral flow direction is parallel to the axis of rotation of the centrifuge which does not produce Coriolis accelerations. However, the settlement component of the deformation will produce some Coriolis accelerations that may bias the direction of the flow but will not directly alter the vertical stresses and run-out distances as described by Bryant et al. (2015).

2.2 Centrifuge container design

The container was required to model a rapid loss of confinement to the contained material and allow observations of the bulk material stability and run-out behaviour. In order to facilitate the design of the novel centrifuge container, the computer-aided design software SolidWorks was utilized (Dassault Systèmes, 1995). This allowed rapid trialling of various container designs and accurate integration of the separate bearing systems, pneumatic and hydraulic actuators within the container and of the container with the centrifuge basket. Figure 1a shows the final centrifuge container design for the run-out experiments. The internal length, width and height of the enclosure for the material are approximately $0.67 \times 0.46 \times 0.4$ m respectively. On opening of the horizontal doors the enclosed material is released onto the plastic run-out basin with a length and width of 1.23 m and 0.98 m respectively. The equivalent field case that the centrifuge container approximates is the breach of a section of a dam or impoundment retaining a material. For example, fig. 1b shows the 1994 Merriespruit tailings dam failure where the failed section is reasonably wide even though it is small relative to the overall width of the pond. In this work the doors open to release material across the entire width of the container. The release of the material in this fashion helps reduce lateral and diagonal fluid gradients which can occur when only narrow or notched openings are modelled (EPRI, 2015), and instead facilitates understanding of the bulk stability of the enclosed material.

An additional benefit to designing the container using SolidWorks was that the elastic deformations of the structural elements could be straightforwardly predicted using the accompanying Finite Element Analyser (Shih, 2014). This was used to ensure plane strain conditions were reasonably enforced prior to the door opening whilst sizing the container side walls and moment connection to the container base plate. Predictions for the 1D lateral strain were at most 0.06 %. Crucially for these experiments, FEA modelling of the door system was also used to conservatively size the door thickness as part of designing the seals for the container doors. Owing to the design featuring a single pin to hold the door closed during the centrifuge experiment - chosen to facilitate faster opening of the doors - the maximum deflections relevant for the seal occurred near

where the bottom of the two doors met.

Figure 2 shows the conservatively predicted deflections (maximum of 5 mm) for the system subjected to a triangularly distributed liquefied soil load at 60 g and full fixity where the system was bolted to the container side walls. To help limit the deflections, the doors had a maximum section thickness of $50.8mm$. This served to reduce both the straining induced in the contained material and the likelihood of leaking prior to the door opening. The door system is also resilient to leaking as the O-ring grooves run along the side faces of the doors, creating a seal between the internal faces of the side walls and container base and the door. This design, comparable to a piston seal, can tolerate larger outward deflection of the doors versus a seal between the front faces of the container and doors.

Further details of the door opening system are described with the annotated photograph in fig. 3a. A single steel pin with a square cross section is used to hold both doors closed. The pin transitions to a circular cross section as it passes through a pair of radial spherical plain bearings in the reaction block and is linked with a shackle to a hydraulic cylinder. Two pneumatic rotary actuators coupled to the door pins are used to accelerate the door opening when the pin is lifted in-flight. The two doors swing open, rotating about pivot points offset from the container walls, to simulate a loss of confinement for the contained material. This design was favoured over sliding doors which shear along the contained material or gates rotating vertically about the top or bottom of the material enclosure. The design objective was to open the doors as rapidly as possible to minimise restricting the subsequent material deformations or flow. A benefit of the horizontal door opening is that if the front face of the material is initially able to keep up with the moving doors, the bias is across the material width and not vertically. The doors' were decelerated and brought to a stop using tetrahedral blocks made of soft modelling clay (fig. 3a). The material and shape were chosen to gradually dissipate the doors kinetic energy as the blocks are sheared, reducing the vibrations imparted to the container as the material run-out progresses.

A consequence of the asymmetric container and model geometry along the bucket is the potential for relative tilt between the bucket and the resultant 'downwards gravitational' force on the model. Figure 3b shows how additional counterbalancing masses were moved to the bucket edge away from the soil container to help mitigate the 'over-tilting' that may otherwise have occurred, depending also on the swing hinge friction. A marble in a grooved, curved track with 0.1° markings was observed in-flight to monitor the resultant bucket tilt during swing-up and prior to the material release. Typically, a bucket tilt within ±1.5° of the ideal value was achieved.

2.3 Instrumentation Placement

Instrumentation within the contained material was achieved using two smooth PVC sheets, spanning the two side walls of the container. Each sheet had portions milled from it using a plastic routing tool to house and guide the instrumentation and cables. A typical arrangement of instrumentation for the run-out testing would be a grid of low-cost pore pressure transducers or tensiometers (Jacobsz, 2018) spanning one wall. These could be used to monitor the water table and dynamic redistribution of pore pressures from the door opening. The individual miniature strain measurement sensor boards were faced with a porous ceramic stone (300 kPa air entry) and cast into epoxy cylinders with reducing radius that could be inserted flush into the plastic side wall. The strain sensor output was calibrated to pressure measurements across a range from -80 to $300kPa$. The stone saturation process, initially consisting of cycles of flushing with CO_2 and applying a vacuum before over-pressuring the stone during saturation was developed based on the recommendations by Take and Bolton (2004). On the opposite wall a grid of moisture content probes, similarly housed within recesses in the plastic, were used to obtain the initial and evolving water content during the material run-out. The complexities of using these probes to infer the water content specific to the fly ash tested are discussed in section 3. External to the contained material GoPro cameras were used to capture videos of the material run-out. In addition, section 4 describes how several depth sensing cameras were installed to image the container and run-out basin, and explores their potential to quantify the material deformations and run-out displacements.

To facilitate future studies on the role of dewatering on the stability of the contained material the container also allows lowering of the water table in-flight, driven by gravity, prior to the doors being opened. Though not utilized in the illustrative centrifuge test results presented in this paper, one design choice for the drainage system should be noted. A large sheet of porous plastic filter material is adhered to the back wall of the container, which also has a port and pneumatic drainage valve near the base (fig. 1a). For fine grained materials, in-flight dewatering is preferable as changes to the centrifugal acceleration will alter the capillary rise and potentially the soil constitutive behaviour if different wetting and drying characteristic curves are traversed (Lu and Likos, 2004). In-flight dewatering prior to the door opening with drainage across the entire back face of the material leads to a consolidation front propagating from the back and top of the material towards the doors and downwards. Nevertheless, a vertical drainage sheet was opted for over a horizontal under-drain to avoid preferential drainage paths from the back of the container to the doors which could occur following the door opening and affect the material run-out.

3 Measuring Water Content: Soil Moisture Probes

The gravimetric water content of a granular material, i.e. the ratio of the mass of water to mass of solids, is an important physical parameter for understanding the material behaviour and can be especially relevant for fine grained materials. In fully saturated materials changes to water content linearly map to changes in voids ratio, and thus determines the drained and undrained shear strengths. In unsaturated soils the water content can also be related to the suctions via the soil water retention curve, and thus the effective stresses and material shear strength. Water contents can be directly measured by fully oven drying samples of material at $110 \pm 10°C$ (or $60°C$ for materials with organic matter) following ASTM-D-2216-98 (1998). However, obtaining the water content of a material within a centrifuge model during testing is less straightforward.

One option is to measure electrical properties of the bulk saturated material, such as it's dielectric permittivity or electrical conductivity, which can be correlated to the gravimetric water content. Kizito et al. (2008) summarise the different categories of soil moisture sensors which rely on these principles, including Time Domain Reflectometry (TDR) sensors, Frequency Domain Reflectometry (FDR) sensors and capacitance sensors. Broadly speaking, Kizito et al. (2008) describe the trade off between the higher accuracy and cost of TDR techniques operating at higher measurement frequencies and the more economical FDR sensors operating at lower measurement frequencies but more readily allowing continuous measurements. Mirshekari et al. (2018) demonstrated the use of a specific dielectric probe also reviewed by Kizito et al. (2008) (EC-5 sensors produced by Decagon Devices) to obtain the soil moisture during dewatering of a level F-75 Ottawa sand bed in a centrifuge test. They emphasised that it was advantageous to calibrate the probes specific to the testing conditions (i.e. soil type, pore fluid and temperature), that the probe alignment (horizontal or vertical) had minimal influence on the readings during calibration and finally that reduced probe accuracy at high saturation values motivates presentation of the results in terms of degree of saturation.

In this work, FDR based GS3 soil moisture probes, a successor to the EC-5 sensors (Meter Group Inc., 2018) that simultaneously measure dielectric permittivity (strictly the apparent dielectric permittivity, a combination of the real and imaginary components), electrical conductivity and temperature, were used. In contrast to the EC-5's flatter dual prong sensors, the GS3 has three circular prongs and a more convenient form factor for use in centrifuge modelling. Further, their smaller detection volume is advantageous for centrifuge models where the stress gradients and thus changes of void ratio and pore fluid distributions can be large. Figure 4a shows a schematic of a GS3 sensor. The probe readings were logged using an SDI-12 to RS323 converter, which was directly connected to a PC serial port during calibration or to a Serial to Ethernet converter for in-flight acquisition on the centrifuge. Section 3.1 details the calibration challenges

of these probes when used with the class-F fly ash tested and section 3.2 illustrates results from run-out centrifuge tests using the same material.

3.1 Calibration with fly ash

The general principle of calibrating the moisture probes is to place the instruments in samples with known water content and correlate this to the measured probe output. In this work individual calibration data was recorded for each probe subsequently used in a centrifuge test. A large sample of oven dried fly ash ($\approx 4\ kg$) was initially taken. Measured volumes of deionized water were mixed into this sample to increment the nominal water content. For each step, a portion was transferred to a smaller container ($\approx 1.5\ kg$) with a known total volume. To avoid interaction with the probes, this was a cylindrical plastic container larger than the volume of influence of the probes. At low water contents the fly ash was tamped into place and at progressively higher water contents it was poured in, with the aim of keeping the sample volume fixed and tracking the bulk density. The output from the probes could then be correlated with the measured water content from oven drying each fly ash sample at $60°C$ over two days, obtained following ASTM-D-2216-98 (1998).

Figure 5a illustrates the outputs from this procedure using an 'as received' probe in the fly ash. Both the measured dielectric permittivity and conductivity are seen to increase non-linearly with increasing gravimetric water content. The limiting probe outputs are also indicated in fig. 5a, that for the permittivity measurement is close to value of 80 which corresponds to the permittivity of water at room temperature. The measured dielectric permittivity in the fly ash saturates the probe output at a water content of about 21 %, though the conductivity measurement was far below the limiting value. The high dielectric permittivity of the fly ash, saturated with deionized water, reduces the usable range of the probe measurement to resolve water contents. The potential of the ionic concentration of the pore fluid to have changed following contact with the fly ash and thus affecting the measurements requires further investigation.

One option to increase the measurement range of the probes within the fly ash is to reduce their sensitivity by covering the prongs with an insulating material. Figure 4b shows example photos of GS3 probes with insulating heat shrink sheaths. Madabhushi et al. (2020) previously reported that this technique could measure water contents up to 28 % in the same fly ash. Figure 5b presents the probe output for the dielectric permittivity and conductivity from a single probe modified in this fashion. It should be noted that by modifying the GS3 probes the recorded outputs can no longer be directly physically interpreted; the on-board electronics for the instruments assume values for the prong sensing length, sensitivity and field distributions. For clarity, the outputs are hence referred to as the indicated dielectric permittivity and

indicated conductivity to distinguish the readings from the 'as received' probes.

Figure 5b additionally indicates the dry unit weight of the fly ash samples each of the probe recordings were obtained from. The liquid limit for the fly ash tested is $\approx 25\%$. Close to and above this value, the dry unit weight necessarily increased with increasing water content, i.e. reducing voids ratio, as the bulk unit weight of the samples could not be controlled. At lower water contents mixing and tamping of the fine grained fly ash samples could yield more uniform dry unit weights, as supported by fig. 5b. Overall, the sensitivity of the probe measurements to the void ratio between samples with the same water content requires further study. The validity of the calibration curves will also depend on the ranges of voids ratio the tested material can achieve at each water content. The calibration data could be more generally applicable for fine grained materials that form a slurry and where the voids ratio depends on the consolidation stresses, i.e. 'clay like' behaviour rather than 'sand like'.

An alternative to using an insulating cover on the GS3 probes to extend the range of measurable water contents from the dielectric permittivity is to reduce the prong length fig. 4c. Figure 6a presents the results from three GS3 sensors using a similar calibration procedure to that previously described. In two of the cases the stainless steel prongs were cut to 10 mm and 20 mm in length. The indicated outputs were also collected over a larger range of water contents. It is immediately apparent that reducing the probe length reduces the capacitance and conductance measured, and thus can extend the range of water contents resolved. A specific benefit of reducing the prong length for run-out tests is the reduced interaction of the sensors with the moving material. An interesting trend revealed by fig. 6a is the rise and then fall of the measured electrical parameters at very high water contents. Whilst the fly ash was largely in suspension at these water contents (i.e. it would eventually consolidate to water contents < 60 %) measurements at these larger water contents could be relevant for understanding the transport and deposition of fly ash in the field (Bachus et al., 2019). If dielectric permittivity measurements are to be used to resolve intermediate water contents, fig. 6a demonstrates the necessity of reducing the probe sensitivity. Such modifications could also be useful for soils which exhibit similar electrical properties to the fly ash, such as soils with natural salts.

All sensors used for the run-out experiments featured a shortened prong length of 20 mm. This represented a balance between the prong length interacting with the moving material and making fuller use of the dielectric permittivity sensing range. Figure 6b presents illustrative calibration data, with the sample dry densities indicated, up to a water content of 30 %. This was the maximum water content expected for the run-out tests presented in this paper. An example of the spline fits used to map the probe measurements to the water contents are also shown. Overall, fig. 6 shows that care must be taken if using the probes over a large range of water contents, as the calibration curve has a non-unique inverse. Further, ranges of the probe output can have plateaus or very shallow gradients making the water content more challenging to

resolve. Nevertheless, the data suggests that over given ranges of water content the dielectric permittivity measurements and/or measured bulk conductivity from the modified probes could be used to obtain the water content from the fly ash or soils with similar electrical properties.

3.2 Illustrative Centrifuge Data

In this section, illustrative results from using the GS3 probes to measure the water content of a fly ash centrifuge run-out test, from the consolidation to door opening stages, are presented. Figure 4c shows a photo of ten modified probes secured in a PVC sheet along the run-out container side wall. The use of plastic straps and nylon bolts to hold the GS3 probes is important to minimize interference with the electrical measurements. Figure 7 presents a cross section of the run-out experiment discussed. The model and prototype dimensions at 60 g are given, in addition to the locations of the ten GS3 probes with respect to the bottom left of the material enclosure. The naming convention refers to the probe column and row index from the same origin. Additionally, the locations of three tensiometers whose data is used to supplement the discussion are shown.

The material used for the run-out tests described is a class-F fly ash (pozzolanic but not diagenetic). For this material, the d_{10} and d_{50} are 3 μm and 21 μm and the plastic and liquid limits are 22% and 25%, respectively (EPRI, 2021, 2015). Further, minimum and maximum dry unit weights from 10.78 to 14.14 kN/m^3 are reported following modified sample preparation procedures described in EPRI (2012). An industrial mixer was used to produce a slurry of the fly ash with deionized water, with a target water content for the slurry of $\approx 30\%$. A forklift was then used to raise the industrial mixer above the centrifuge container and the fly ash was sluiced into the container through an outlet at the bottom of the mixer. A single pour of the material was left to consolidate at 1 g for $>$ 24 hours. The final material heights of 20.8 m and water table position of 22.8 m at 60 g, before the doors were opened, are indicated in fig. 7. An approximation of the dry density from the bulk material mass, height and container volume suggested a value of 14.95 kN/m^3. Though slightly larger than the maximum density previously reported, the sensitivity of the density calculations to the sample mass and material height must also be acknowledged. Overall, that the sample preparation resulted in a relatively dense deposit of saturated fly ash should be concluded. As a result, it may anticipated that the material may be relatively stable and exhibit limited run-out as static liquefaction of the deposit is unlikely.

The calibration data discussed in section 3.1 suggested the indicated dielectric permittivity and indicated conductivity could be independently used to infer the material water content. To explore this, fig. 8 presents the calibration measurements from four probes with a prong length of 20 mm and the data obtained during a

centrifuge run-out test. Starting with the calibration data, the changes to the measured dielectric permittivity and measured conductivity are plotted against each other for four different probes, revealing a non-linear relationship as both quantities depend on the changing water content. However, overlaying the centrifuge data from the same probes shows significant deviation of the relation between the simultaneously measured quantities, particularly at indicated conductivities below $6000\mu S/cm$. Ultimately, whilst both measurements are physically correlated with the water content, fig. 8 shows at least one quantity may not be reliably used to interpret the centrifuge test data using the 1 g calibration results. In this project, the water contents inferred from the bulk conductivity measurements were found to agree more closely with pre and post test sampling from the centrifuge testing. Values derived from the indicated dielectric permittivities yielded lower water contents, consistent with the data in fig. 8. The importance of verifying indirect measures of the material water content, particularly for centrifuge modelling tests, is exemplified.

From first pouring of the fly ash slurry and 1 g consolidation through to the centrifuge flight and door opening the GS3 probes were logged. The manner in which the probes were sequentially logged limited the sampling rate to $\approx 0.1Hz$ during the centrifuge test. Figure 9a presents the time history of these events, in terms of the measured conductivity from the ten modified probes and inferred water contents. Broadly, the time histories in fig. 9a show that the water content was initially high after the slurry was deposited, rapidly decreasing and also becoming more uniform with time at 1 g. On opening of doors fig. 9a shows there is a staged drop of water contents within the material.

In fig. 9b the time histories of inferred water contents from selected GS3 probes are presented alongside the pore pressures obtained from a column of tensiometers near the opening doors (locations in fig. 7). Figure 9b shows the pore pressures quickly equilibrating with increases to the g level and remaining constant until the doors are opened. The hydrostatic pore pressures confirm the fly ash fully consolidated as the model was swung up. However, significant reductions to the void ratio and thus water content are not suggested by the inferred water contents. Following the door opening, the drops in water content in the material near the door are accompanied by rapid reductions of pore pressure and even temporary suctions closer to the fly ash surface. It is noted that the tensiometers were only calibrated to $\approx -80\ kPa$, and thus a horizontal cut-off line is plotted in fig. 9b to indicate greater measured suctions may be unreliable / indicate de-saturation of the stones that had an air entry value of 300 kPa. Section 4 contains further interpretation of these coupled water content and pore pressure changes in conjunction with the measured material movements.

Further insight can be made by examining the distributions of water content constructed from this data at several instants of time (fig. 9c). The measurement values and linear interpolations of the data points (in recognition of the lack of a predictive model for the water content distributions) are shown. For simplicity, all values are plotted at the final prototype locations. It is confirmed that on first pouring of the slurry

there was a spatially variable water content across the material. Figure 9c highlights how at the end of the 1 g consolidation the pore fluid had redistributed and the water content was quite uniform along and with height through the contained material. Prior to the door opening at 60 g, a slight reduction in water content at all locations, in line with the expected consolidation of the material under it's self weight, can be discerned. Table 1 shows the statistical mean and range of water contents from all ten sensors at these three stages of testing. On opening of the doors, there appears to be an immediate and fairly uniform reduction of water content at all locations, again confirmed by the values in table 1. This may be associated with the initial water flow but also a bulk settlement and horizontal expansion of the fly ash mass as the horizontal confining stress from the doors is removed. In addition to the small drop at all locations, there is larger gradual reduction of water content, propagating from the front right of material that be can be clearly visualised. Section 4 uses the rate of observed water content changes and redistributions, coupled with the pore pressure time histories and depth camera data, to gain insight into the deformation mechanics of the material run-out.

Overall, following the careful modification and calibration of the GS3 probes, the data presented illustrates how unique insight into the spatial and time varying distribution of the water content within the material can be made. For saturated fine grained materials, the water content can be an effective proxy for the voids ratio and undrained shear strength. Such probes can be used to determine the water content across and with depth through the model at both 1 g and on the centrifuge. That this is achieved without intrusive sampling is especially advantageous, allowing unique judgements on the model preparation and uniformity to be made. Further, for run-out experiments the evolution of the water content distributions can be used to gain insight into the progressive deformation mechanisms.

4 Profiling the Run-out: Depth Sensing Cameras

There exists a variety of methodologies to obtain the material deformations in small scale centrifuge tests. Direct point measurements of displacement, particularly for structural elements or the soil surface, can be achieved with traditional instrumentation such as Linear Variable Differential Transformers (LVDTs) or drawstring potentiometers. Planar deformations of large areas of material can be obtained using Digital Image Correlation techniques, which rely on locating the same region of material between successive 2D images (Stanier et al., 2015). This methodology has also been demonstrated to work in 3D with multiple cameras, for example to track the out of plane settlements of a curved and submerged slope surface (Stone, 2019). However, a drawback of these techniques can be the computational time and effort of post processing the images, in addition to the direct hardware cost.

In this work, the performance of multiple low cost depth sensing cameras are explored. A key advantage of these 'off the shelf' cameras is their ease of inclusion in a centrifuge tests, internal and automatic calibration of the depth information captured and minimal post-processing required. The specific model of cameras used was the D435 Intel® RealSense™ Depth Sensing Camera, pictured in fig. 10a (Intel®, 2018). The distance or depth of objects from the camera is calculated using the principals of stereoscopic depth rendition, i.e. comparison of the relative positions of the same object captured by two cameras a known distance apart. This calculation is performed on-board the D435 cameras and the resulting ROSBAG output was processed using a combination of MATLAB and Python libraries.

$$\alpha_{x/y}(z_i) = \frac{FoV_{x/y}}{2} + \arctan\left(\tan\left(\frac{FoV_{x/y}}{2}\right) - B/z_i\right) \tag{1}$$

$$\Delta x = \frac{z_i}{\tan\omega_{ix}} \tag{2a}$$

$$\omega_{ix} = A_x + \frac{sh_{ci}}{n_c}\alpha_x(z_i) \tag{2b}$$

$$\Delta y = \frac{z_i}{\tan\omega_{iy}} \tag{2c}$$

$$\omega_{iy} = A_y + \frac{sh_{ri}}{n_r}\alpha_y(z_i) \tag{2d}$$

Equation (1) shows the relation given by Intel® (2018) for the field of view for the depth sensing cameras, which is a function of the distance of the object to the plane of the camera module in addition to the individual field of view of each depth imager and separation between them. Figure 10b defines the variables and also illustrates how the resulting depth image with pixel coordinates can be straightforwardly converted to a point cloud in real space using the equations shown in eq. (2), assuming linear divisions of the fields of view over the depth image.

4.1 Illustrative Centrifuge Data

As part of the centrifuge run-out tests previously described, multiple depth sensing cameras were installed at the locations highlighted in fig. 10a. The potential for these cameras to provide information about the flow of the material from the container to the run-out basin and the resulting profile of the material is explored. During the centrifuge test the depth information was captured at a frame rate of 30 frames per second at a resolution of 848×480 px. As previously described, as the test features an initially dense fly ash deposit a limited collapse without static liquefaction of the material may be anticipated.

In fig. 11 illustrative point cloud reconstructions from the depth sensing cameras are shown. Two time instants are presented, illustrating the versatility of the cameras to capture material deformations at relatively short and long model time scales. In fig. 11a, the initial material movements ≈ 1.5 s after the door opening are shown, alongside a corresponding still image of this instant. Visually, the opened doors, run-out basin and relatively vertical wall of outward moving material have been reasonably captured. The ability of the dense saturated fly ash to transiently maintain a steep, > 10 m tall face suggests negative excess pore pressures are generated in the short term, supported by the measurements in fig. 9b. The eventual collapse and progressive outward movements of the fly ash in this test is clearly visualized in fig. 11b, approximately 20 minutes in model time after the initial door opening.

As a note on the accuracy of the depth sensing cameras, the manufacturer's reported error is up to 2 % of the measured depth. For the typical camera placements in the run-out test this implies absolute errors up to 8 mm and 25 mm for the closest and farthest cameras respectively, or up to 0.45 m and 1.4 m for scaling at 60 g. Whilst these values represent the maximum errors they would suggest the measured deformations cannot replace existing two-dimensional digital image correlation techniques, especially to calculate strains. Notwithstanding this, the relative cost and convenience of the depth sensing cameras, especially to capture large-scale three-dimensional movements of relatively untextured materials in centrifuge tests, can justify their use. The on-board automatic calibration of the depth information output also adds to their convenience. However, as this is completed at 1 g the potential for the self weight of the camera components to induce distortions and errors to the stereoscopic depth rendition should also be acknowledged. As an initial exploration of the cameras accuracy during the centrifuge test, table 2 presents the theoretical and reconstructed dimensions from the depth sensing cameras' of relatively rigid container components. The mean, total standard deviation and number of measurement points used are also indicated. The theoretical and measured values are in good agreement at the prototype scale and with reasonably small standard deviations. The various components or distances referenced were located at a range of depths within the point-cloud and no systematic errors are obvious. Whilst this is not a comprehensive review of the camera accuracy, there is no strong evidence to suggest the increased self weight of the depth sensing camera components during the centrifuge test significantly worsens the manufacturer's stated accuracies.

Based on symmetry, the central portion of the released material can be approximated to have plane strain conditions. Following the construction of the point clouds at each time instant as illustrated in fig. 11, the profiles of material movement into the basin can be extracted. Figure 12 presents the averaged profiles over the central 0.5 m of measurements in the initial 5 s after the doors were opened (fig. 12a) and the progressive movements captured over 20 minutes model time (fig. 12b). In fig. 11a the immediate outward movement of the fly ash body can be observed; initially a steep face that collapses in two stages leading to farther material

movement into the basin and shallower standing faces within the original deposit. In fig. 12b the continued longer term deformations of the fly ash are visualized. It is evident that whilst the material continues to move from the container to the run-out, and in general reduce the gradient of the sloped faces, the process happens in discrete stages.

The use of depth sensing cameras to visualise the moving front of material has been clearly demonstrated. However, a distinction between the use of the depth sensing cameras in this way versus digital image correlation techniques should be made. Large deformations can be tracked at modest frame rates as captured objects or unique regions do not need to be identified and tracked through sequential images. However, a disadvantage of only obtaining the moving front of material is that the relative displacements of a soil region and hence Lagrangian velocities cannot be straightforwardly calculated from the depth data alone. The scope to combine the depth data with the visible light images from the same cameras and digital image correlation techniques to obtain relative displacements, and potentially velocities and/or strains, will be explored in future works.

Nevertheless, the profiles measured can be used to calculate the evolution of the total volume of material in the run-out basin and combined with other instrumentation to gain insight into the overall deformation mechanics. For example, fig. 13 presents the time histories of the fly ash water contents, pore pressures and computed volumes of material. The values shown in fig. 13a were calculated using numerical integration of the point cloud data at prototype scale and feature the time histories of the total volume of material measured in the run-out and lost from the original deposit from multiple cameras. The overall trend of both traces adds weight to the previously described time scales of the material movements; immediately after the doors are opened there is an outward movement of material which is transiently stable. The following material movements do not appear to occur continuously, but rather sudden collapses of the steeper faces leads to abrupt volume changes with intermittent periods of stability.

Combining the volume calculations with the changes to the water content and pore pressures on the same time scales, as shown in fig. 13b and fig. 13c, can provide further insight into the deformation mechanics. It is however important to note only measurements from the un-collapsed material can be obtained, as guided by the comparisons shown in fig. 12. Compared to fig. 9b in particular, fig. 13c shows with dashed lines the pore pressure measurements after the material moves away from the sensors and the measurements may only reflect desaturation of the porous stones. Distinguishing between material suctions and the sensor desaturation is an additional benefit of combining the pore pressure measurements with the depth sensing camera data for problems modelling large material movements.

Overall, the larger volume computed in the run-out than calculated to have been lost from the container, particularly shortly after the door opening, may be attributed to dilation of the deforming material as well as

to errors associated with the volume calculations. Material dilation is supported by the previous bulk density estimates and transient stability of the material, where the development of negative excess pore pressures within the material may have helped temporarily support the steep faces. It is clear however that the initial progression of the collapse is not accompanied by a large change in water content, with only MP3 − 4 at the top right corner of the contained material exhibiting a slight reduction in the first 1 min. In contrast to this, there is a large and continual reduction of water contents at both MP3 − 4 MP3 − 3 that precede a major material collapse at approximately 3.5 min after the door opening. This data further supports the redistribution of pore fluid being the cause of the continued collapses of the slopes.

The increased difference between the run-out and material exited volumes following the major material collapse at approximately 3.5 min corresponds to an increase of ≈ 35 % of volume in the run-out; likely too large to be solely attributed to dilation. As an initial estimate of the calculated volume error, based on the camera manufacturer's error of up to 2 % of the depth measured the volume error will be within -5.9 % to 6.1 %, i.e. an error of ≈ 240 m^3 for a calculated volume of 4000 m^3. An additional source of error may be the piles of dry blocks of material in the run-out basin that may not be solid masses, as assumed for the volume calculations, but may also have entrained air. Similarly, the decrease after 18 min is physically unlikely to be due to material contraction and more likely due to a combination of the errors discussed and possible movement of material out of the field of view of the cameras.

5 Conclusions

High quality physical testing data is needed by a number of industries concerned with the deformation mechanics and subsequent run-out behaviour of saturated granular materials. Centrifuge modelling can provide a relatively inexpensive route to capture the effective stress driven physics of the material deformations in reduced scale models. In this paper, the design and capabilities of a novel centrifuge container to model a rapid loss of horizontal confinement for the contained material is presented.

The application of two different instrumentation techniques to better characterize the run-out, with illustrative centrifuge data, has also been considered. Soil moisture probes that measure the apparent dielectric permittivity and conductivity have been used to infer the spatial and time varying distributions of water content during the deposition of the fly-ash and in-flight. The high dielectric permittivity of the saturated fly ash necessitated reduction of the measurement sensitivity, for example by reducing the probe length, to avoid sensor saturation. Further, discrepancies between the water contents inferred from the indicated dielectric measurements and indicated electrical conductivities were demonstrated between the 1 g calibration data and centrifuge results. Careful calibration of the sensors with additional direct determination

of the tested material water content was necessary for reliable use of these instruments with the fly ash investigated. The present study suggests attention should be paid to the bulk density of the material, in addition to the soil type and pore fluid highlighted by previous studies, during the sensor calibration.

The use of low-cost depth sensing cameras to capture the fly ash deformations was also successfully demonstrated. The cameras allowed the three dimensional movements of the fly ash front to be straightforwardly reconstructed both immediately after the door opening and over a longer time scale. The magnitudes and progression of the deformations were captured and enabled calculation of the total volume of material movement and an indication of the shear induced volume changes. Coupled with the water content and tensiometer measurements, the combined datasets gave unique insight into the both the short and longer term deformation mechanics of the initially dense fly ash subject to a rapid loss of confinement. It is anticipated the water content and depth measurement techniques will usefully supplement traditional sensors in future centrifuge testing.

6 Acknowledgements

The complex centrifuge tests described would not have been possible without the technical and moral support from Chad Justice, Tom Kohnke, Anatoliy Ganchenko and Mary Carrillo at the UC Davis Center for Geotechnical Modeling. The financial support and guidance from the Electrical Power and Research Institute (EPRI) was also essential. The help from Undergraduate Research Assistants Kevin Chavira, Saman Lavasani and Henry Wijaya, in addition to Jasmin Lugo supported by the NHERI REU program, is also gratefully acknowledged by the authors. Finally the assistance from the UC Davis Granular Mechanics Lab, in particular Kyle O'Hara and Lin Huang, is appreciated.

References

ASTM-D-2216-98 (1998). Standard Test Method for Laboratory Determination of Water (Moisture) Content of Soil and Rock by Mass, *ASTM International* (January): 1–5.

Bachus, R. C., Terzariol, M., Pasten, C., Chong, S. H., Dai, S., Cha, M. S., Kim, S., Jang, J., Papadopoulos, E., Roshankhah, S., Lei, L., Garcia, A., Park, J., Sivaram, A., Santamarina, F., Ren, X. and Santamarina, J. C. (2019). Characterization and Engineering Properties of Dry and Ponded Class-F Fly Ash, *Journal of Geotechnical and Geoenvironmental Engineering* **145**(3).

Been, K. (2016). Characterizing mine tailings for geotechnical design, *Proceedings of the 5th International Conference on Geotechnical and Geophysical Site Characterisation, ISC 2016* **1**: 41–55.

Bishop, A. W. and Blight, G. E. (1963). Some aspects of effective stress in saturated and partly saturated soils, *Geotechnique* **13**(3): 177–197.

Bowman, E. T., Laue, J., Imre, B. and Springman, S. M. (2010). Experimental modelling of debris flow behaviour using a geotechnical centrifuge, *Canadian Geotechnical Journal* **47**(7): 742–762.

Bryant, S. K., Take, W. A., Bowman, E. T. and Millen, M. D. (2015). Physical and numerical modelling of dry granular flows under Coriolis conditions, *Geotechnique* **65**(3): 188–200.

Dassault Systèmes (1995). SolidWorks.

Delaney, K. B. and Evans, S. G. (2014). The 1997 Mount Munday landslide (British Columbia) and the behaviour of rock avalanches on glacier surfaces, *Landslides* **11**(6): 1019–1036.

EPRI (2012). Geotechnical properties of fly ash and potential for static liquefaction: volume I–summary and conclusions, *Technical report*, EPRI, Palo Alto, CA.

EPRI (2015). Centrifuge Models of Embankment Failures on Saturated Coal Ash, *Technical report*, EPRI, Palo Alto, CA.

EPRI (2021). Geotechnical Centrifuge Tests to Assess Stability of Slurry-Deposited Coal Fly Ash, *Technical report*, EPRI, Palo Alto, CA.

Intel® (2018). Intel® RealSense^{TM} D400 Series Product Family.

Jacobsz, S. W. (2018). Low cost tensiometers for geotechnical applications, *Physical Modelling in Geotechnics - Proceedings of the 9th International Conference on Physical Modelling in Geotechnics 2018, ICPMG 2018*, Taylor & Francis, London, UK, pp. 305–310.

Johnson, B. C., Campbell, C. S. and Melosh, H. J. (2016). The reduction of friction in long runout landslides as an emergent phenomenon, *Journal of Geophysical Research: Earth Surface* **121**(5): 881–889.

Kizito, F., Campbell, C. S., Campbell, G. S., Cobos, D. R., Teare, B. L., Carter, B. and Hopmans, J. W. (2008). Frequency, electrical conductivity and temperature analysis of a low-cost capacitance soil moisture sensor, *Journal of Hydrology* **352**(3-4): 367–378.

Lu, N. and Likos, W. J. (2004). *Unsaturated Soil Mechanics*, Wiley.

Madabhushi, S. S. C., O'Hara, K., Martinez, A. V., Wilson, D. W., Boulanger, R. W., Kutter, B. L. and Ladwig, K. (2020). Centrifuge Modeling of Fly Ash Deposit Dewatering, *Geo-Congress 2020*, Minneapolis, pp. 20–28.

McDougall, S. (2017). 2014 canadian geotechnical colloquium: Landslide runout analysis — current practice and challenges, *Canadian Geotechnical Journal* **54**(5): 605–620.

Meter Group Inc. (2018). GS3 Integrator Guide.

Mirshekari, M., Ghayoomi, M. and Borghei, A. (2018). A Review on Soil-Water Retention Scaling in Centrifuge Modeling of Unsaturated Sands, *Geotechnical Testing Journal* **41**(6): 20170120.

Pinyol, N. M., Alvarado, M., Alonso, E. E. and Zabala, F. (2018). Thermal effects in landslide mobility, *Geotechnique* **68**(6): 528–545.

Schofield, A. N. (1980). Cambridge Geotechnical Centrifuge Operations, *Géotechnique* **30**(3): 227–268.

Shih, R. H. (2014). *Finite Element Analysis Using SolidWorks Simulation 2014*, SDC publications.

Stanier, S. A., Blaber, J., Take, W. A. and White, D. J. (2015). Improved image-based deformation measurement for geotechnical applications, *Canadian Geotechnical Journal* **13**(October 2015): 1–35.

Stone, N. S. (2019). *Tracking 3D Displacements of a Submerged Liquefied Surface Using Multiple Cameras*, PhD thesis, University of California, Davis, Davis.

Tailings.info (n.d.). Aerial view of the Merriespruit tailings dam Disaster.

Take, W. A. and Bolton, M. D. (2004). Tensiometer saturation and the reliable measurement of soil suction, *Géotechnique* **54**(3): 229–232.

List of Figures

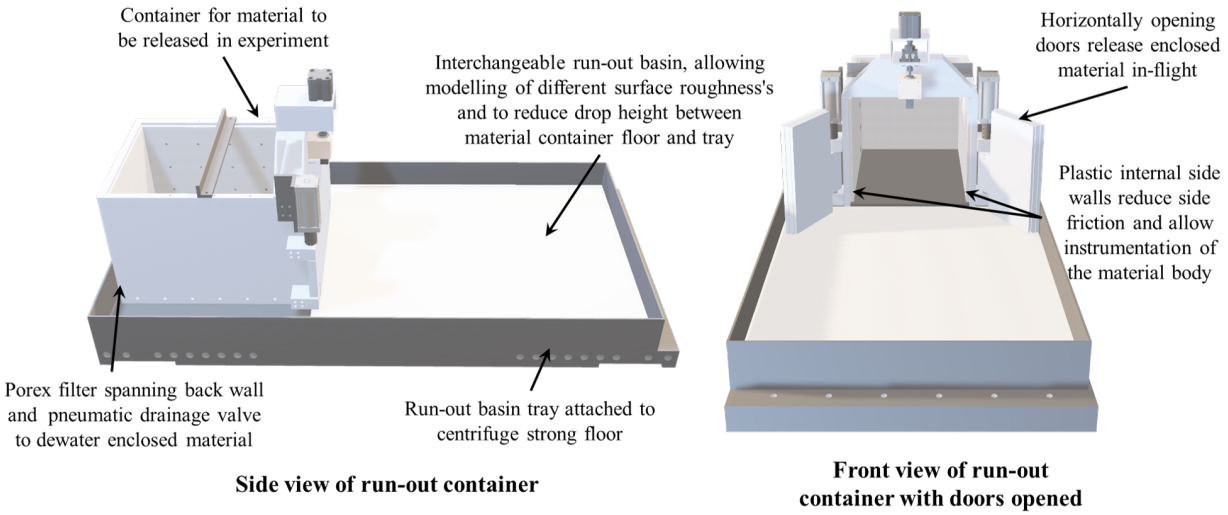

(a) 3D CAD model and details of container for run-out experiments

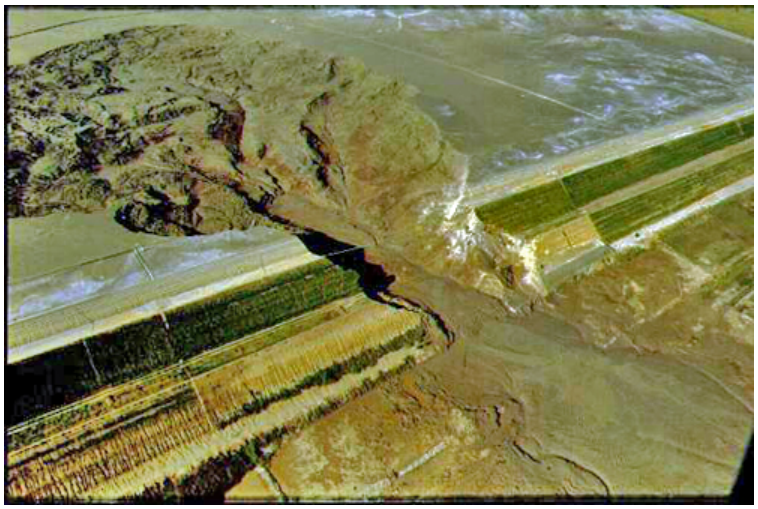

(b) Merriespruit tailings dam failure, an example of the type of run-out problems the novel centrifuge container can help model (Tailings.info, n.d.)

Figure 1: Design of the novel centrifuge container used to conduct run-out experiments and example of equivalent field case that the centrifuge container models

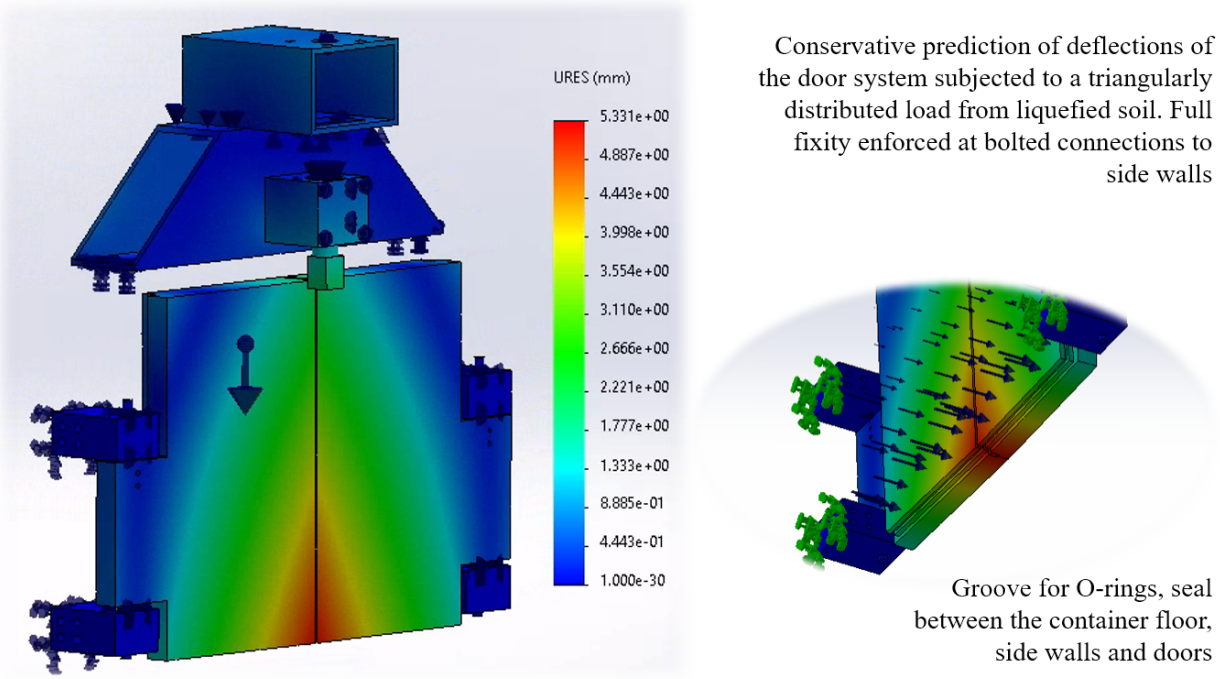

Figure 2: Illustrating the use of SolidWorks FEA to conservatively predict the door deflections if the container is filled with liquefied material at 60 g in order to the design the door seals

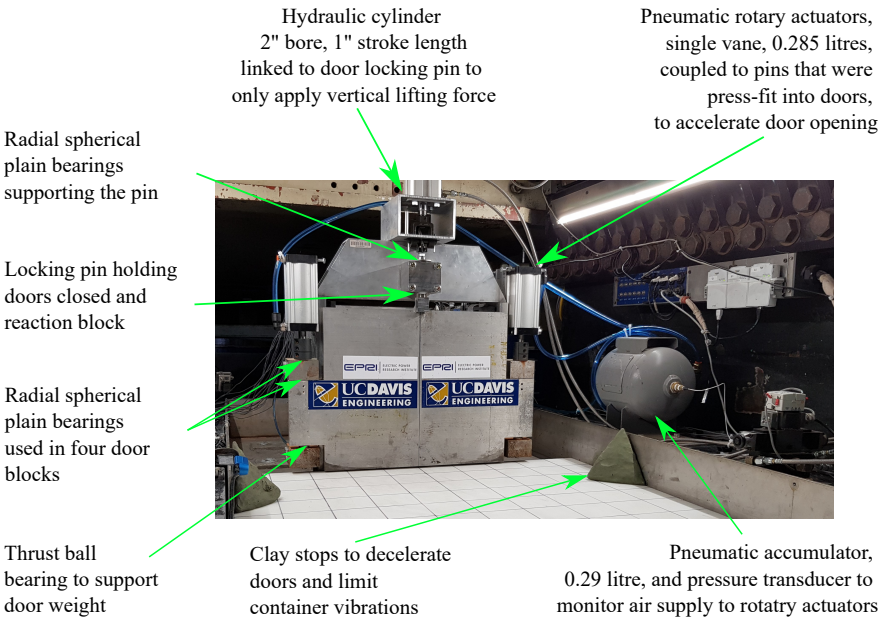

(a) Photo with details of the door opening mechanism and associated mechanical, hydraulic and pneumatic systems with the container loaded on the UC Davis 9-m centrifuge

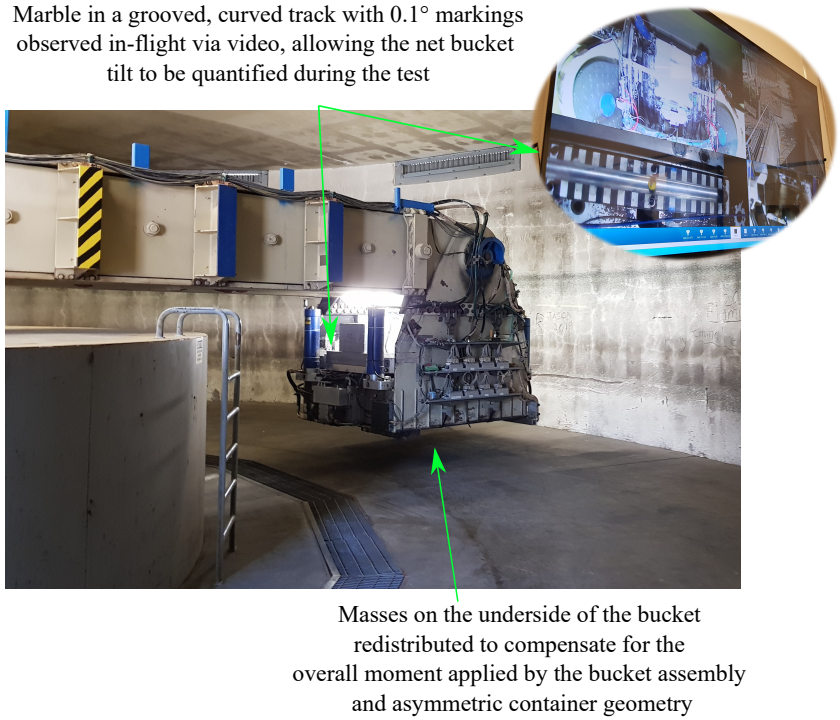

(b) Photo illustrating adjustment of the bucket balance to compensate for the asymmetry of the run-out container and simple system to estimate the net bucket tilt in-flight

Figure 3: Photographs of novel run-out container loaded on the UC Davis 9-m centrifuge, details of the door opening mechanism, associated systems and efforts made to balance and verify the bucket tilt in-flight

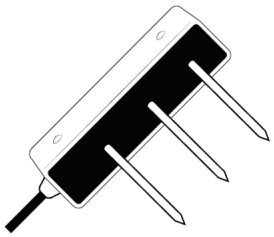

(a) Schematic of unmodified ECH_2O GS3 moisture probes following Meter Group Inc. (2018)

(b) Modified probes using heat-shrink as an insulating cover over the stainless steel electrodes and vertical arrangement as used in Madabhushi et al. (2020)

(c) Modified probe array with reduced length of the stainless steel electrodes without insulating covers and grid arrangement as used in the run-out tests

Figure 4: Schematic of the unmodified GS3 moisture probes and photographs of various modifications made to the probes to improve their performance when used in centrifuge tests with the saturated fly ash

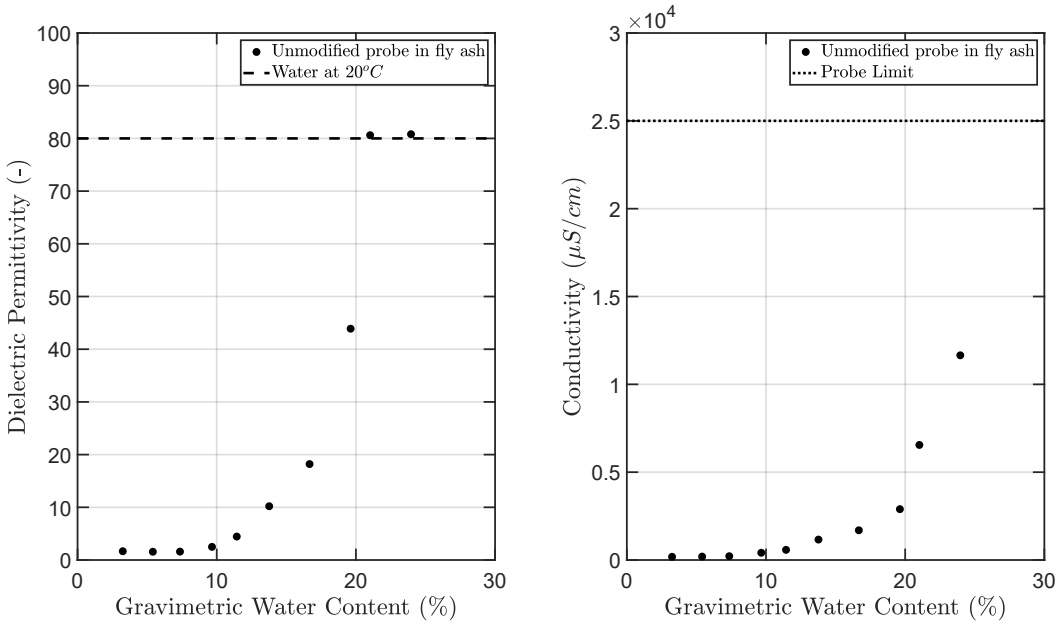

(a) Instrument outputs from unmodified or 'as received' probe in terms of electrical properties measured versus gravimetric water content of the fly ash

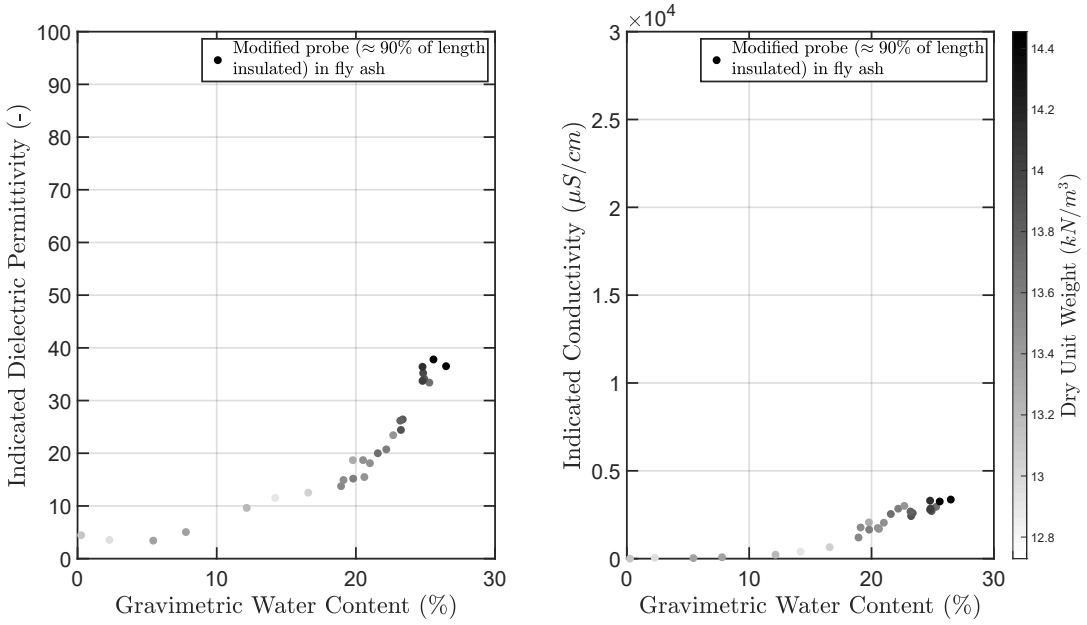

(b) Modified probe output; indicated electrical properties from probes with insulating covers versus gravimetric water content of the fly ash

Figure 5: Illustrative GS3 probe outputs for initial calibration trials in fly ash showing increased sensing range of water contents from the indicated Dielectric Permittivity if the probes are modified using an insulating cover

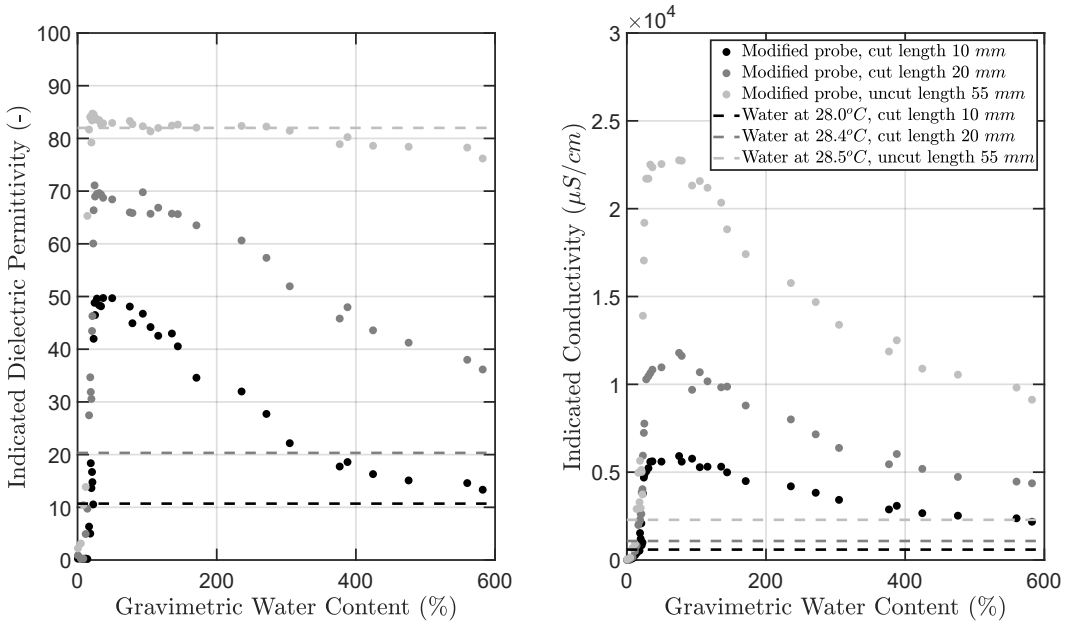

(a) Modified probe output; indicated electrical properties from probes with reduced length versus gravimetric water content of the fly ash

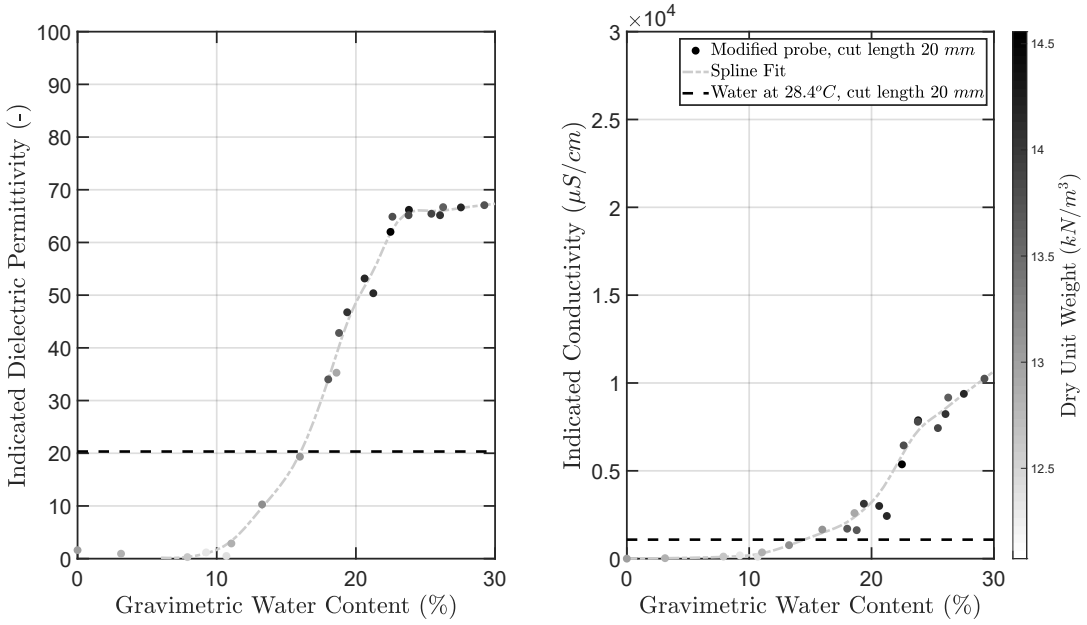

(b) Close up of modified probe output results over expected range of interest for centrifuge run-out tests and fitting curves used to infer water content

Figure 6: Illustrative GS3 probe outputs for secondary calibration trials in fly ash; increased sensing range of water contents achieved in this case by reducing the probe length which is also beneficial for reducing interaction between the material and instrument during the run-out tests

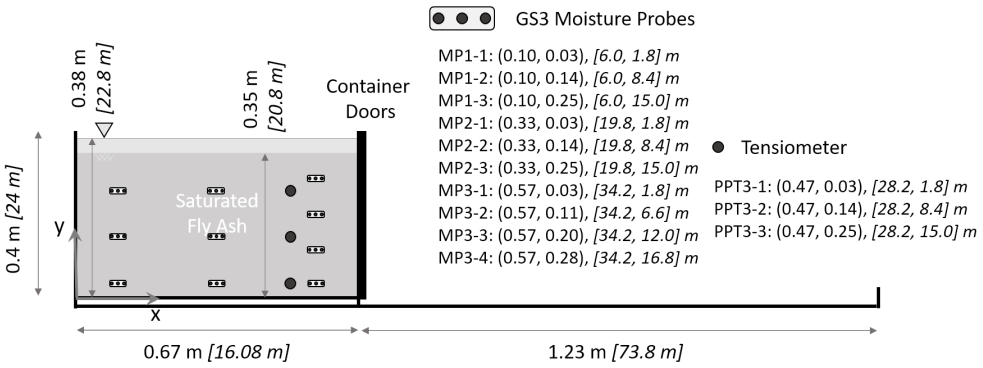

Figure 7: Cross section of centrifuge run-out test, model and 60 g prototype dimensions, and instrumentation locations for results discussed in this work

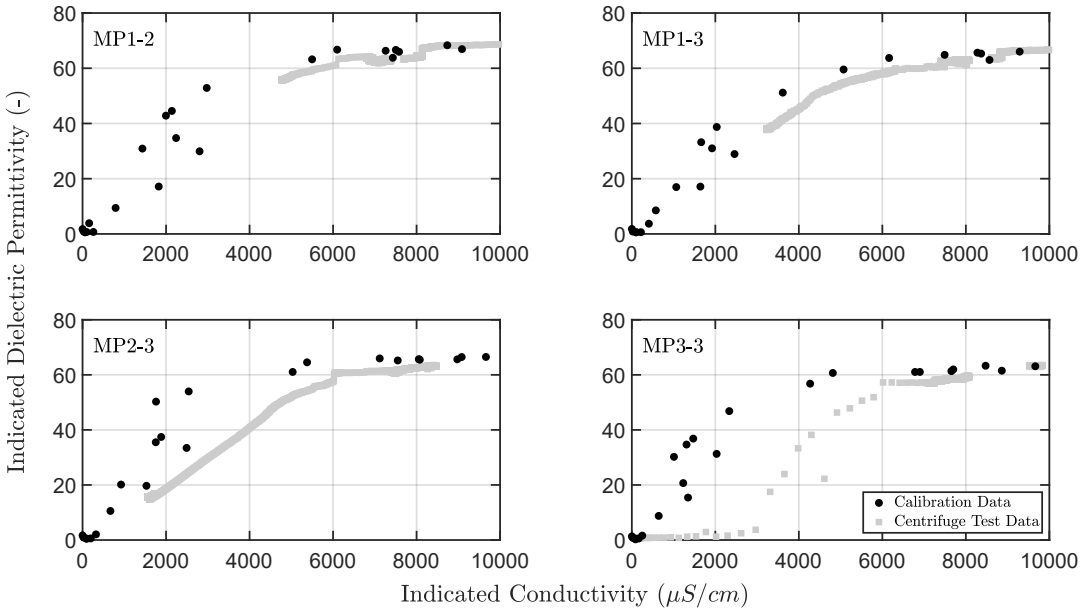

Figure 8: Data from four modified probes revealing a different relationship between the measured dielectric permittivities and measured conductivities from changing water contents during calibration versus centrifuge testing

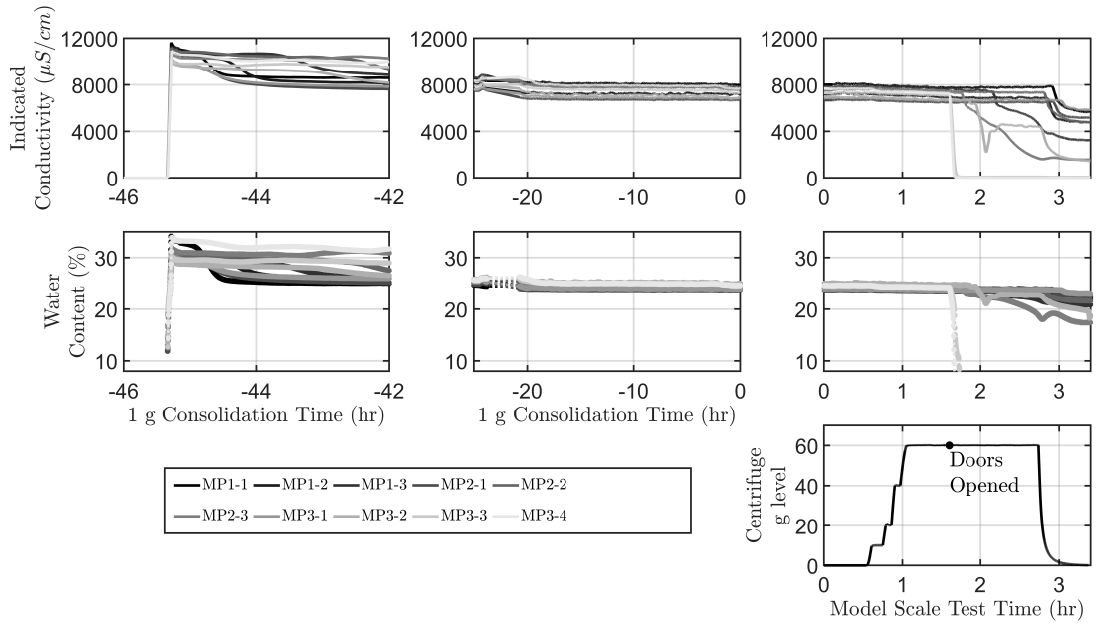

(a) Time history of water contents inferred from measured conductivities spanning the initial model preparation and centrifuge run-out test. The uniformity of the water contents prior to the door opening is verified by these measurements

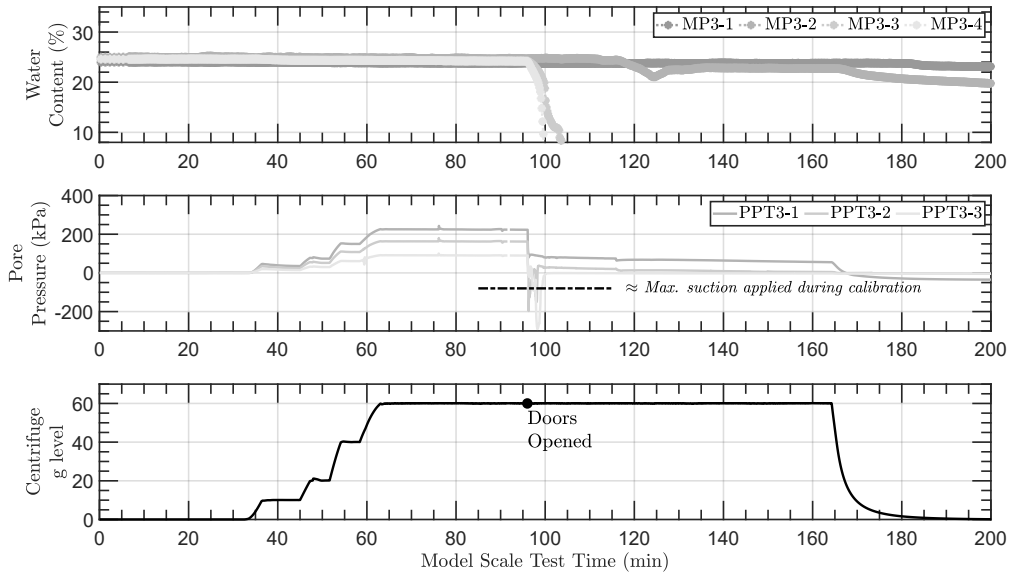

(b) Time history of water contents and pore pressures from instruments near the door opening showing material consolidation during swing up with concurrent reduction of water contents and temporary generation of negative excess pore pressures following the door opening

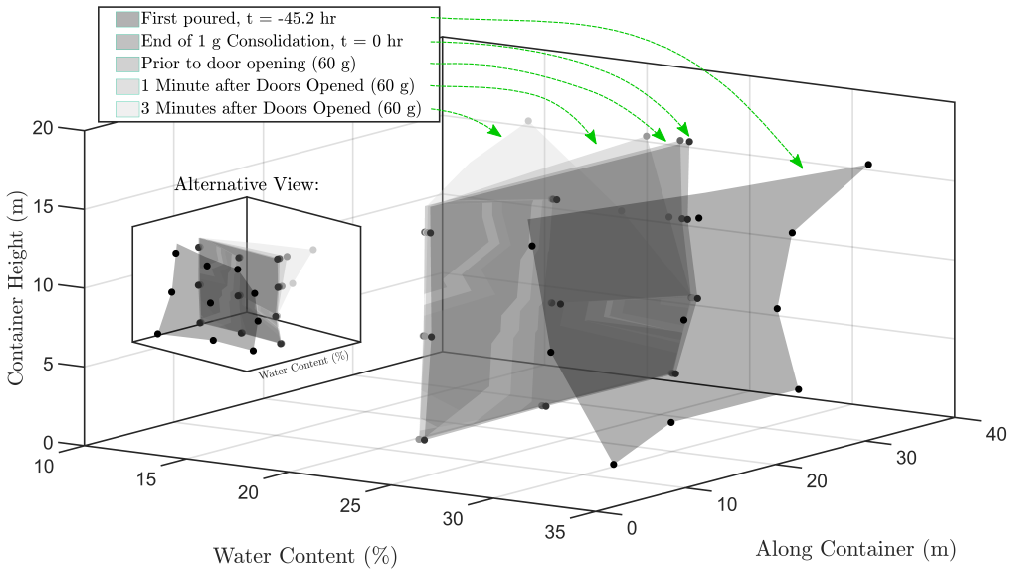

(c) Distribution of water contents inferred from measured conductivities at the final prototype scale, confirming the uniformity of the water contents prior to door opening followed by a rapid and uniform reduction of water contents and progressive reduction of water contents from the top right of the released material

Figure 9: Illustrating the data collected from the GS3 probes, with both model time histories and prototype distributions facilitating insight into the initial uniformity and progression of water content within the model across the preparation and run-out processes

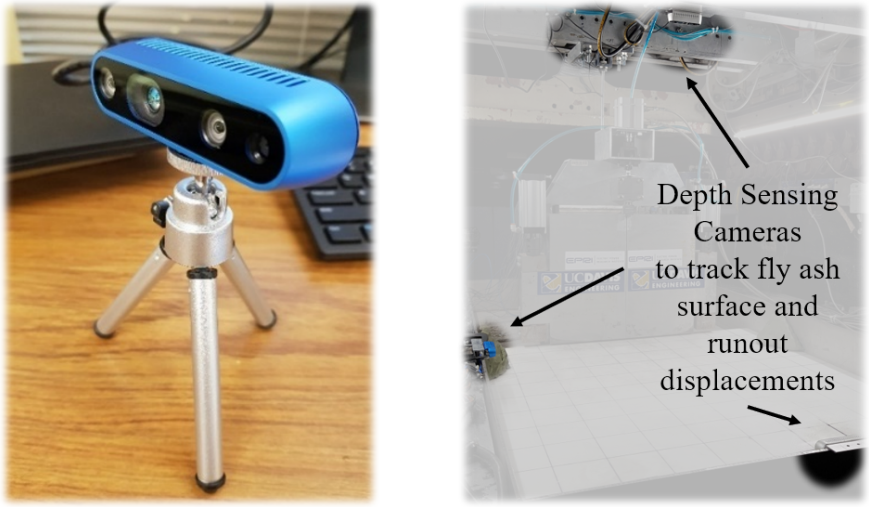

(a) Intel® RealSense™ Depth Sensing Cameras close up (left) and arrangement of multiple cameras to capture depth data during the run-out tests (right)

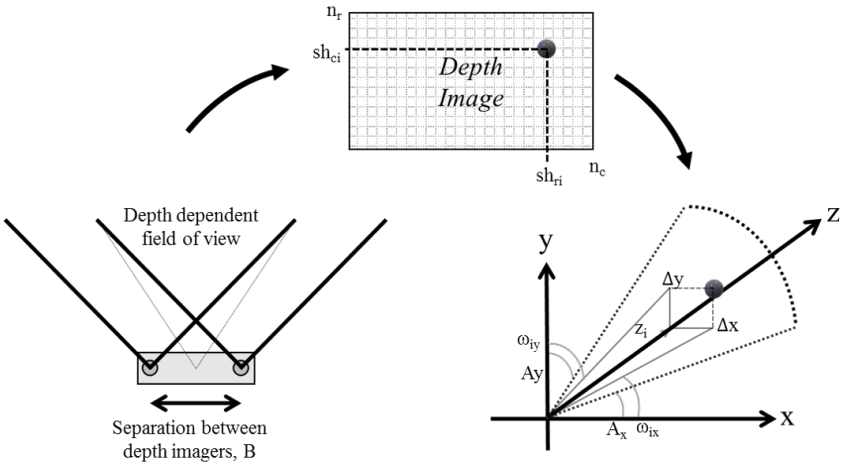

Symbol	Definition
A	External angle to field of view
$n_{r/c}$	Number of rows / columns in depth image
$sh_{r/ci}$	Row or column index of pixel in depth image
α(z)	Depth dependent field of view
z_i	Normal depth of object from camera plane
ω_i	External angle to object location

(b) Geometric details and notation for distances and angles used to construct three dimensional point cloud from the depth images captured

Figure 10: Detailing the arrangement and geometric details of the depth sensing cameras used to reconstruct the material front prior to and during the centrifuge run-out tests

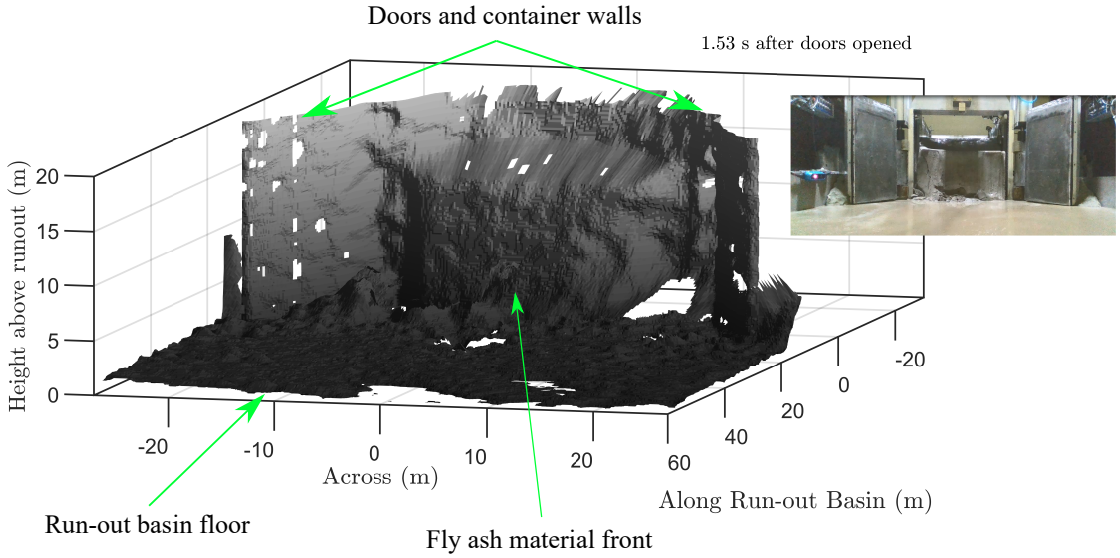

(a) Time instant showing initial container and prototype material movements ≈ 1.5 *s* after the door opening - the fly ash is transiently maintaining a steep, tall face of material

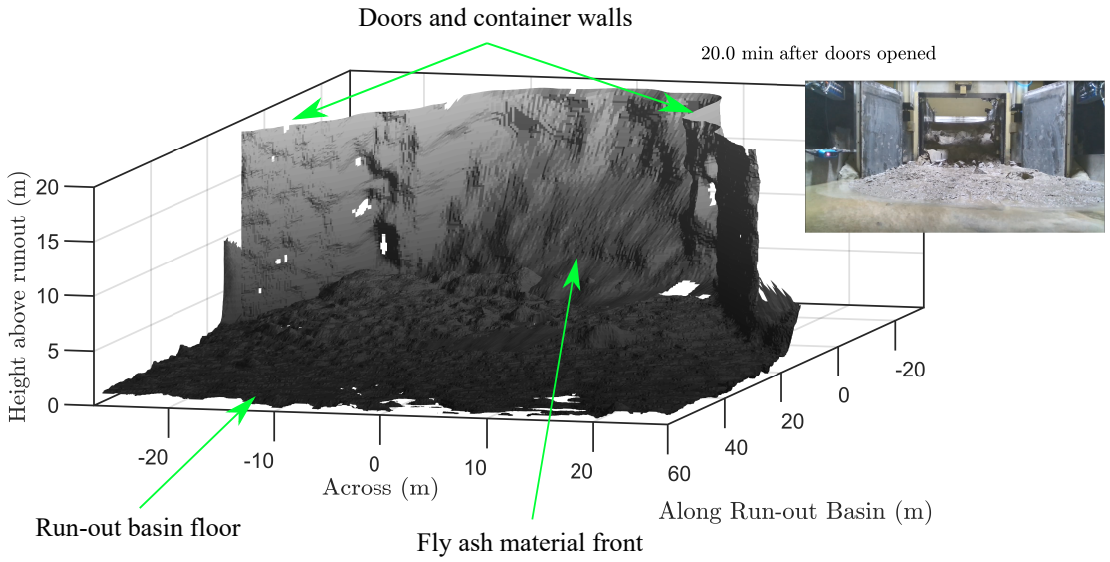

(b) Time instant showing container and longer term prototype material movements ≈ 20 *min* after the door opening showing gentler slopes of the fly ash following the collapse of the steep faces

Figure 11: Illustrating point cloud reconstructions from multiple depth sensing cameras used during centrifuge run-out tests to capture the material front immediately after the door opening and resulting deformations in the longer term

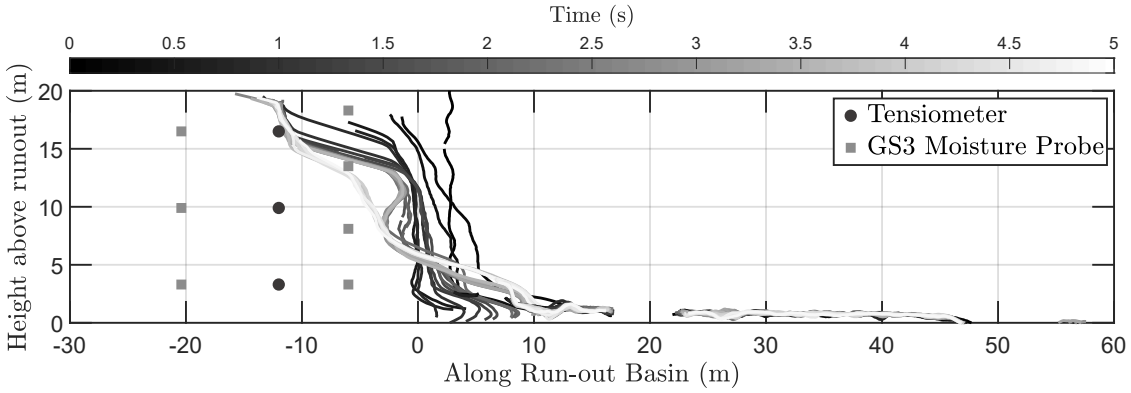

(a) Central profiles of material movement captured during from the first 5 s model time of the run-out event, highlighting the immediate outward movement and staged collapse of the steep faces

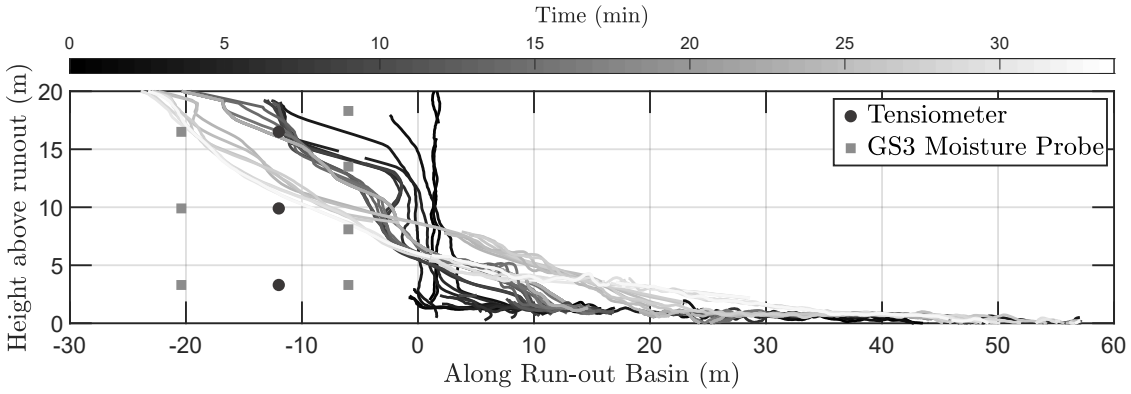

(b) Central profiles showing the progression of the longer term material movement and gradual reduction of the steeper slope angles up to ≈ 30 min model time after the door opening

Figure 12: Illustrating extracted central profiles of material movement at prototype scale from multiple depth sensing cameras showing the immediate and longer term progression of material movements. Locations of tensiometer and GS3 probes along container (negative abscissa) and run-out basin (positive abscissa) are additionally shown

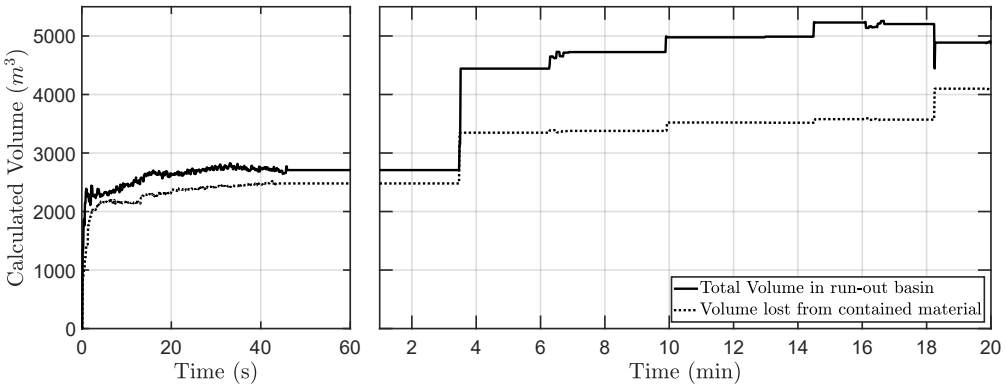

(a) Volume of material in the run-out tests calculated from the depth sensing camera measurements, highlighting the sudden collapses of material followed by periods of intermittent stability and potential indications of deformation induced volume change of the material

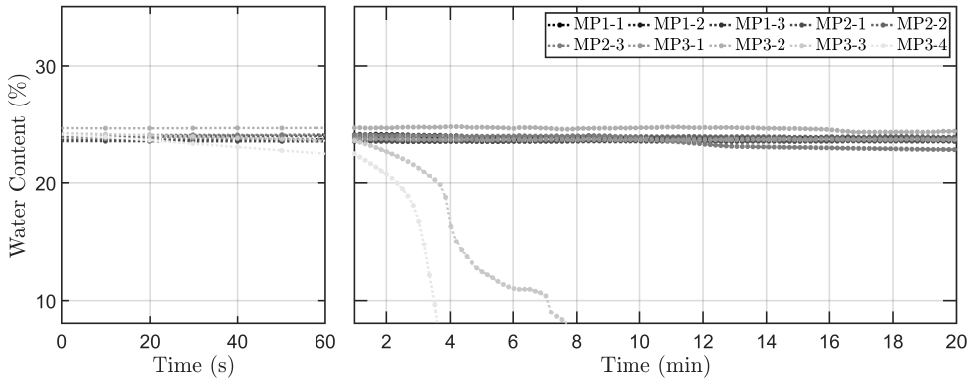

(b) Time history of water contents following the door opening event showing water content changes occur more gradually than the material movement

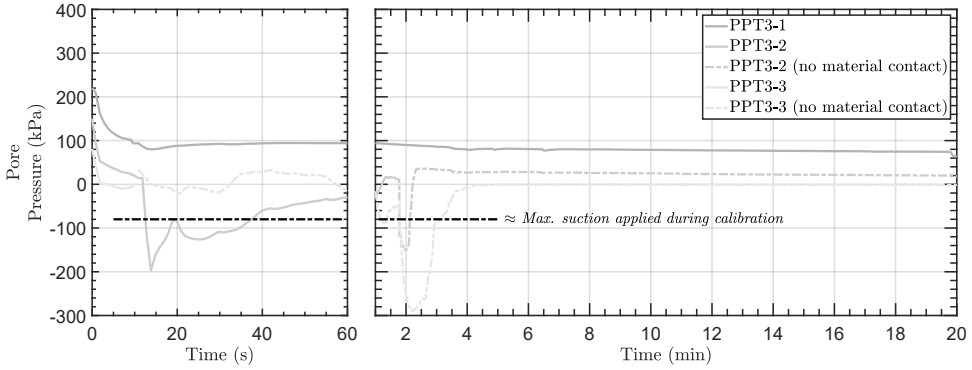

(c) Time history of pore pressures following the door opening event showing rapid changes in response to the door opening

Figure 13: Combining instrumentation to examine the time scales of material and pore fluid movement in the run-out tests supporting rapid generation of suctions leading to intermittently stable material faces which collapse and move outwards as the pore fluid gradually and continually redistributes

List of Tables

Table 1: Examining the distribution of water contents using the GS3 probe data

Time	Mean Water Content (%)	Range of Water Contents (%)
First Pouring	30.61	4.45
End of 1 g Consolidation	24.33	1.25
Prior to door opening (60 g)	24.05	1.12
1 minute after door opening (60 g)	23.83	2.19

Table 2: Exploring the accuracy of the point-cloud reconstructions of the centrifuge run-out test at prototype scale

Component or Distance	Theoretical (m)	Mean measured value (m)	Standard Deviation of measured values (m)	Number of Points
Run-out basin width	59.2	58.8	0.59	9378
Separation between pneumatic actuators	32.4	30.7	0.19	37
Width of contained material	23.6	24.2	0.24	156
Height to pin cross bar assembly	27.8	26.3	0.21	499